High-fidelity light curve simulation and validation using empirical data

Tristan Meyer, Denise Keil, Daniel Traub, Stefan Scharring
Wolfgang Riede, Thomas Dekorsy
German Aerospace Center (DLR), Institute of Technical Physics

Max Nussbaum
DiGOS Potsdam GmbH

Michael Lengowski, Robin Schweigert, Sabine Klinkner
University of Stuttgart, Institute of Space Systems (IRS)

ABSTRACT

The growing number of objects in orbit creates a pressing need to improve space situational awareness. In-orbit missions have the potential to contribute to a sustainable space environment by maintaining, repairing, or removing defunct space objects. To conduct such missions, it is essential to know the rotational behavior of the target object beforehand. Dynamic object information can be obtained through ground-based measurements by the acquisition and analysis of light curves from observations of sunlight which is reflected from d ebris. S ubsequently, f or a n in-depth characterization of the object's rotational state, these measurements are correlated with simulated data. Our simulation framework computes synthetic light curves on the basis of radiometric quantities. Therefore, it is well suited for in-depth characterization of space objects. In this study we aim to validate our simulations exhibiting an absolute sensor response with light curve observations of the Flying Laptop satellite, which is operational and, thus, can be used for light curve assessment and analysis. The simulations are incorporated with spectral laboratory measurements of the reflective behavior of common spacecraft materials, in order to produce high-fidelity si mulations. A powerful tool in further characterizing cataloged objects are reflectivity maps that project the reflected sunlight intensity of the object via the phase vector into a body-fixed f rame. Reflectivity maps are unique for each individual object and only need to be simulated once, reducing the computational effort of light curve analysis. This technique is illustrated with the Flying Laptop satellite, by matching measurements with the simulated map. Reflectivity maps have the potential for fast attitude assessment via light curves for objects with known geometry and composition, paving the way for light curve inversion, e.g., for attitude determination.

1. INTRODUCTION

The largest population of space residential objects can be found in the regions near 450 km, 800 km, and 1200 km. The 800 km orbit is historically popular, while 450 km and 1200 km just recently became crowded due to the launches of mega-constellation satellites. Since the launch of the first patch of StarLink satellites in 2019 the number of active objects in space increased by a factor of 6 [1]. In addition, to the approximately 9800 active satellite missions, there are more than one million space debris objects, among them numerous defunct satellites, spent rocket bodies, and a vast multitude of fragments, which are not serving any purpose but causing threat to active missions [2].

Collisions in space pose a severe threat to a sustainable orbit, creating potential risks for active satellites. Historically most prominent is the Cosmos-Iridium-Collision, which is a major fragmentation event and caused approximately 1300 additional cataloged debris fragments [3]. In order to minimize the risk of such events, close observation of the orbital situation - SSA (Space Situational Awareness), and further actions - STM (Space Traffic Management), are required [4]. Hence, the orbital situation is constantly monitored by radar and optical observations [5]. Data is further processed to generate conjunction warnings in case of a close approach of two or more objects. The immense increase of objects in space since the rise of the New Space Age leads to an overload of collision warnings [4]. The estimated annual economical losses due to collisions with space debris are in the range of $86 - $103 million [6]. As

a result, operators often have to maneuver their satellites to avoid collisions, which incurs a cost of $700 to $1300 per maneuver, depending on the mission (excluding human space flight) [7].

Such events create a pressing need for servicing and removal of critical space debris objects. To address this task, active removal missions are being developed that shall capture and deorbit critical space debris. Prominent examples are the ELSA-d and Adras-J missions pursued by the Japanese company Astroscale, aiming for commercial in-orbit servicing and removal services [8]. Moreover, the ESA (European Space Agency) is contributing to a sustainable orbit developing the debris removal mission Clearspace-1 [9]. Nevertheless, in order to safely capture these objects without generating even more debris, the rotational state of the object has to be known in advance.

A popular tool to analyze a space object's rotational state are light curves - time-resolved brightness information of an observed target. Changes in attitude may lead to characteristics in the light curves, e.g., a specular reflecting surface will cause a peak in the signal. Depending on the attitude, i.e., rotational motion of an object, the peak or any other visible features will occur periodically during the time of observation.

In-depth characterization of unknown parameters of the space object can be achieved by matching light curve simulations to the respective measurements. Reconstructing an object's characteristics, such as the rotational behavior, material abundance, and shape from light curves, is known as the inversion problem. However, due to the large parameter space dictating measured light reflections, signal inversion attempts are generally ill-posed. Therefore, researchers often require a priori information and large datasets to be able to extract unknown attributes from the targets. In the case of removal or servicing missions, the rotational state is the characteristic of interest. In order to minimize the unknown parameter space and, thus, accurately tackle the inversion problem, prior information regarding the dimensions and materials are favorable.

Current light curve simulations for space objects lack validation of radiometric output. In [10] for example the ground-truth BRDF (Bidirectional Reflectance Distribution Function) was measured for the CanX-1 satellite. In addition, the multispectral BRDF was modeled and compared to the measurement. It showed that no quantitative comparison was possible, since the simulation did not output radiometric quantities. Nevertheless, a qualitative comparison succeeded. In [11], on the other hand, good agreement between the model and measurements was found for the Lageos satellite, which is a simple sphere made of metal. Moreover, it has been demonstrated that the relative magnitude for an ATLAS 5 upper stage shows good agreement with measurements. This was shown for relative magnitudes, therefore, lacking radiometric output. Wang et al. [12] have established a laboratory set-up of a scaled Galileo satellite. Measuring and simulating the irradiance, it was possible to validate their model with an error of 11 %. However, real life measurements and comparisons of space objects have not been conducted.

At the DLR (German Aerospace Center) Institute of Technical Physics competencies in light curve measurement including operation of telescope stations, cleanroom-based material characterization, and light curve simulations are combined. Having the University of Stuttgart's IRS (Institute of Space Systems) in close neighborhood, we have great opportunities for investigating a well-known space object: the Flying Laptop satellite [13]. In the past, Nussbaum et al. [14] demonstrated that our in-house light curve software Raxus Prime is capable of correctly simulating the measured signal count, by fitting the albedo of simple spherical satellites, Calsphere 4A and LCS 1. The current work aims to validate Raxus Prime simulations with complex geometries, several installed materials and complex material distributions on the satellite. Hence, the materials of the mainly visible areas of the Flying Laptop have been investigated by measuring their respective specular reflex and roughness characteristics. Both pieces of information were used to generate a BRDF based on microfacet theory. In parallel, light curves of the Flying Laptop were taken in campaigns in 2019 and 2024 by our stations UFO (Uhlandshoehe Forschungsobservatorium) and miniSLR. Attitude data, where available, was provided by the IRS. Subsequently, it was possible to compare simulated and measured light curves for validation purposes. Finally, the Flying Laptop's reflectivity map is computed, which is used to illustrate light curve assessment and compared to conventionally simulated data.

2. METHODS

First of all, we provide an overview of the materials and methods used in this study, covering an introduction of the Flying Laptop satellite, the lab set-ups and measurements of the integrated materials, the light curve simulation framework, as well as the BRDF model that is embedded in the simulations and parameterized by the lab-measurements.

2.1 The Flying Laptop Satellite

The Flying Laptop is a small satellite developed by the University of Stuttgart's IRS in Germany and launched into a 600 km sun-synchronous orbit on July 14, 2017, from the Baikonur Cosmodrome in Kazakhstan. The objectives of the Flying Laptop mission are to demonstrate various satellite technologies, conduct Earth observation as well as serve educational means. In the area of technology evaluation, for example, an optical downlink to a ground station was verified in cooperation with the DLR, a new type of avionics was space-tested, and an innovative low shock deployment mechanism was demonstrated. In addition to optical scientific Earth observation using two camera systems, the satellite also monitors global shipping traffic via an AIS (Automatic Identification System) receiver in cooperation with the DLR. The satellite has a mass of approximately 110 kg and a size of 1.9 x 0.8 x 0.7 m^3 in the deployed configuration (Fig. 1). Developed, built, and operated by PhD, graduate and undergraduate students with assistance by partners of industry, such as Airbus DS and Tesat Spacecom, as well as research institutions, the Flying Laptop has been operated for seven years via the University's control centre and ground segment and is still operational.

Fig. 1: Picture of the Flying Laptop satellite in the deployed configuration [15].

The satellite's design concept combines the traditional and new space approaches. As a result, the satellite platform has been composed with full redundancy from a combination of reliable and high-performance old space components and cost-effective new space components. The satellite has a 3-axis attitude control system, utilizing no propulsion system. The average pointing accuracy during a pass over the ground station in target pointing mode is less than 100 arc seconds with a pointing knowledge in the range of a few arc seconds [13].

In addition to its sophisticated design, the satellite's surface materials have been studied in our cleanroom environment in order to gain realistic spectral and roughness data as an input for our simulations. The present work contains the outer layer of the applied MLI (Multi-Layer Insulation) stack (coated polyimide with front-sided indium-tin-oxide and backsided aluminum), unidirectional CFRP (Carbon-Fiber Reinforced Plastic), a triple junction solar cell, structural parts of untreated aluminum, and brushed copper.

2.2 Lab measurements

In order to provide input data of real surfaces into the light curve simulations, we took spectral reflectance measurements for each material. Furthermore, we measured the surface roughness of the samples. Both types of measurement data are a required input parameters for the BRDF model, which will be described in subsection 2.3.

2.2.1 Spectrometric measurements

Measurements of specular reflectance spectra were obtained with a Bruker Vertex 70v Fourier-Transform Infrared spectrometer. The spectrometer is equipped with a mirror stage that allows for measurements with an AOI (Angle of Incidence)/AOR (Angle of Reflectance) of 30°. This angle is assumed to be the most common reflection angle of sunlight to the observer, neglecting the changes in the reflectivity due to its angular dependency. As a light source we applied a tungsten filament source combined with a silicon diode as a detector. Measurements are calibrated with a gold mirror standard. Errors due to absorption losses at the gold mirror for wavelengths below 600 nm are compensated by a correction with the true gold spectrum retrieved from its wavelength-dependent refractive index [16]. The measured spectra of the materials are shown in Fig. 2.

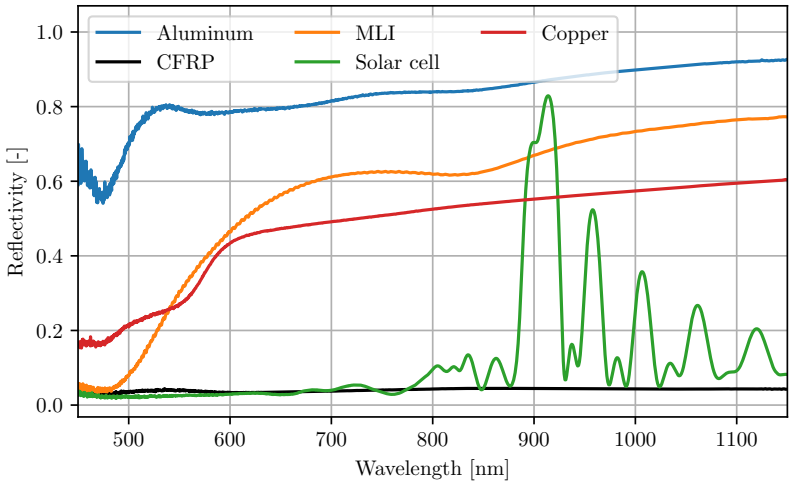

Fig. 2: Results of specular reflectance measurements at 30° AOI/AOR comprise the following materials: Outer layer of the Flying Laptop's MLI hull, Flying Laptop's solar cell panel structure made by unidirectional CFRP, Solar Cell, comparable to those installed on the Flying Laptop satellite, aluminum representing parts of the structure, brushed copper sheet metal depicting the DDS (Direct Digital Synthesizer) antenna and for reference purposes.

2.2.2 Surface Roughness

We measured surface roughness of the Flying Laptop samples using a WLIM (White Light Interferometer), Bruker Wyko NT9100 equipped with the standard camera with 640 x 480 pixels. This instrument allows for interference-based surface profiling. An area of 0.5 x 0.6 mm was measured at a sampling resolution of 971 nm. The respective roughness maps are displayed in Fig. 3.

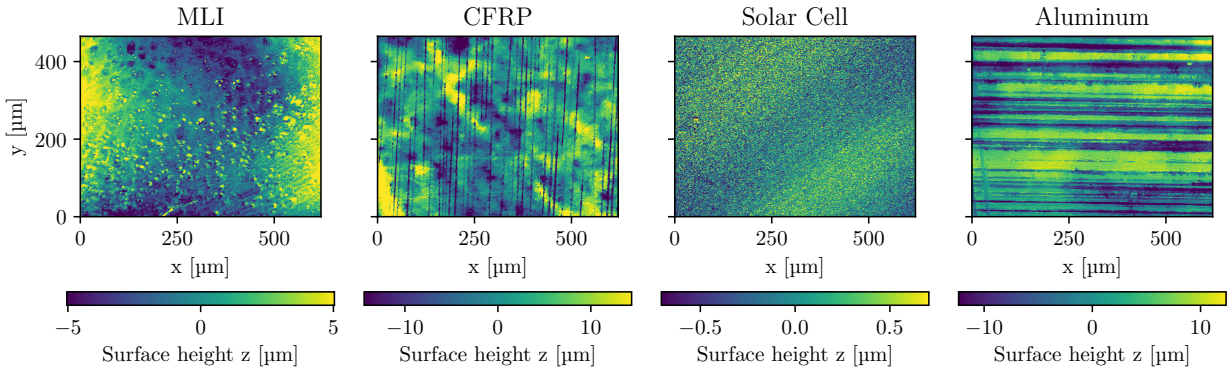

Fig. 3: Roughness maps of the investigated materials obtained via WLIM. **Left to Right:** Outer layer of the Flying Laptop's MLI hull, Flying Laptop's solar cell panel structure made by unidirectional CFRP, Solar Cell, comparable to those installed on the Flying Laptop satellite, aluminum representing structural components.

The copper sample is excluded in this case, since only a brushed copper piece was available. This unfortunately does not represent the copper DDS antenna on the Flying Laptop satellite, therefore, it is only used to measure the spectrum.

2.3 Light curve simulation and BRDF model

The light curve simulation framework is based on the Raxus Prime light curve simulator, originally developed by Daniel Burandt [17] at the Institute of Technical Physics and subsequently enhanced by Ewan Schafer and Max Nussbaum [18, 19]. Raxus Prime facilitates the simulation of spectral light curves in units of radiance, incorporating

wavelength-dependent radiation transfer effects and accounting for accurate instrument transmissions and detector quantum efficiencies. Additionally, it includes the consideration of realistic material reflections. The simulation is carried out in three principal steps [14]:

1. Geometric relations between light source, e.g., Sun, target and observer are propagated from a target's TLE (Two Line Element) and rotational parameters or attitude information.
2. Reflections are computed by rendering the geometry at discrete time intervals during the pass and subsequently fused to form a spectral light curve.
3. Additional processing steps are applied to the series of spectral data such as atmospheric attenuation and conversion to instrument responses.

The spectral renders are performed using the Mitsuba2 opens-source render engine [20], which implements a classical Monte Carlo ray tracer, featuring a range of sampling strategies to ensure the efficiency of computations. Atmospheric attenuation is accounted for by the radiative transfer library libRadtran [21], which was developed as open-source software at the DLR in Oberpfaffenhofen. Raxus Prime exploits the library to compute transmission spectra in the wavelength resolution of the render at each observation geometry.

Scattering properties of surfaces are generally characterized by the BSDF (Bidirectional Scattering Distribution Function), which accounts for effects of reflective as well as transmissive materials [22]. Common spacecraft materials such as solar panels, MLI or aluminum permit little subsurface transmission. Therefore, light interactions are captured solely through reflective effects using a subset of the BSDF, namely the BRDF, which is defined as the ratio of reflected radiance $L_o(n_o,\lambda)$ to incident irradiance $E_i(n_i,\lambda)$ on a macro surface [22]

$$f_r(n_i,n_o,\lambda) = \frac{dL_o(n_o,\lambda)}{dE_i(n_i,\lambda)}. \tag{1}$$

The distribution of surface reflections, thus, makes up a five-dimensional problem that varies with the wavelength λ as well as directions of incident n_i and outgoing n_o light. Beyond the object's orientation and dimensions, the BRDF plays a pivotal role in the simulation and analysis of light curves. Integration of BRDFs into light curve simulations can be achieved through two main approaches: utilizing measured BRDFs or employing empirical and analytical models. The current version of our light curve software Raxus Prime incorporates an analytical BRDF model, a modified version of the Cook-Torrance model [23], seamlessly integrated within the Mitsuba2 rendering engine. The model accounts for specular and diffuse reflectance. In short it can be written to [23]:

$$f_r(n_i,n_o,\alpha,\lambda) \propto F(n_i,\lambda)G(n_i,n_o,\alpha)D(\alpha). \tag{2}$$

The term $F(n_i,\lambda)$ is the Fresnel term, accounting for the wavelength-dependent reflection. $G(n_i,n_o,\alpha)$ and $D(\alpha)$ are statistical functions that describe the geometric attenuation and slope distribution of the microfacets, respectively [23].

Equation 2 is based on a macroscopic level, where the individual terms $G(n_i,n_o,\alpha)$ and $D(\alpha)$ are derived from the statistical distribution of the microfacets normals (m) and their corresponding incident and outgoing rays (w_i, w_o), as illustrated in Fig. 4.

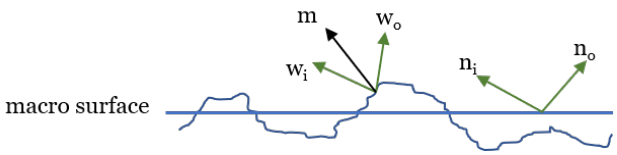

Fig. 4: Illustration of microfacets with normal vector m, incident direction w_i, and outgoing direction w_o, such as the vectors for the macro surface n_i and n_o, respectively.

Various statistical microfacet distribution functions, such as Beckmann, GGX, and Phong [23] exist for consideration. In this research, the Beckmann distribution for the $G(n_i, n_o, \alpha)$ and $D(\alpha)$ term is employed, contingent upon the statistical value of the RMS (Root Mean Square) slope α of the microfacets.

A common method to determine α is to statistically analyze the surface profile $z(x,y)$ of a material, as conducted for the samples shown in Fig. 3.

In order to determine α, two statistical measures are relevant. The RMS height R_q of the material and the autocorrelation length τ, which results from the autocorrelation function $\Delta(\delta x, \delta_y)$ (see Equation 3). The autocorrelation function characterizes the random nature of a surface profile and the relative spacing, i.e., shift distance in x and y direction (δx, δy) of peaks and valleys. A represents the area of the probe in both dimensions.

$$\Delta(\delta x, \delta y) = \iint_A z(x,y) z(x+\delta x, y+\delta y) dx dy \tag{3}$$

The autocorrelation length τ is defined as the minimal shift distance from the zero shift where $\Delta(\delta x, \delta y)$ drops below 20 % in any direction [24]. In Fig. 5 the two-dimensional autocorrelation maps resulting from the measured MLI and CFRP are shown. Since MLI is a rather smooth material, the RMS height deviation R_q results in 2.9 µm. The autocorrelation length τ is 140 µm. The values for the CFRP result to 8.63 µm for R_q and τ to 37.2 µm. This behavior is also visible in Fig. 3. Due to the increased randomness of the height profile of CFRP, $\Delta(\delta x, \delta y)$ has a narrow peak, thus, dropping off rapidly, in comparison to the rather smooth MLI.

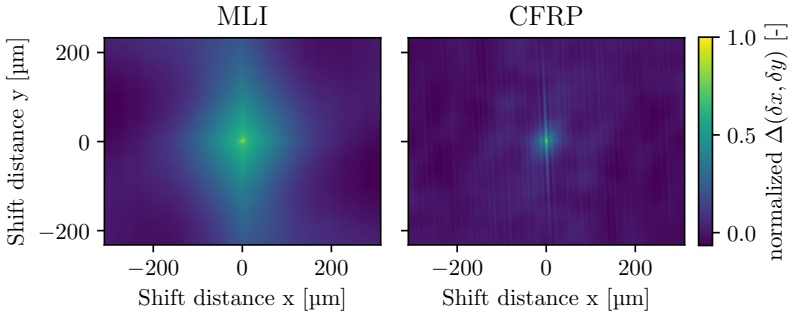

Fig. 5: Resulting two-dimensional autocorrelation function $\Delta(\delta x, \delta y)$ from the measured roughness of the MLI and CFRP sample, respectively.

The slope of a rough surface in the case of the Beckmann microfacet distribution, can be taken as the ratio of the RMS height deviation R_q to the autocorrelation length τ, namely, $\alpha = \sqrt{2} R_q / \tau$, which is valid for Gaussian roughness assumptions [22, 25]. In the case of the shown MLI probe, α results to 0.03 and for the CFRP probe to 0.326. The statistical values and the resulting slopes for the other measured material samples are listed in Table 1.

Table 1: Statistical values R_q, τ and the resulting slope α of the measured materials.

Material	RMS height deviation R_q [µm]	Autocorrelation length τ [µm]	RMS slope α
MLI	2.93	140	0.0295
CFRP	8.63	37.2	0.326
Solar Cell	0.341	1.814	0.265
Aluminum	5.33	14.7	0.513
Copper[1]	5.33	14.7	0.513

[1] Values for copper are assumed to be identical as aluminum, since no actual probe from the Flying Laptop is available.

In combination with a reflectance spectrum, measured as described in subsubsection 2.2.1, the Fresnel term can be defined [23], and the material's distinctive BRDF can be modeled using Equation 2.

3. STUDY

This section provides the details of the light curve simulations and measurement observatories of the DLR. Additionally, a brief explanation is given on how the intensities are extracted from the light curve measurements.

3.1 Simulation

Light curve simulations with Raxus Prime are carried out in a wavelength range from 450 nm to 1150 nm in 5 nm bins.

Orbit data is provided by the most recent TLE from the epoch of observation downloaded from [26]. Attitude data is provided by the IRS, originating from the star trackers of the satellite, within the accuracy as described in subsection 2.1. The attitude is used, in order to correctly simulate the relative attitude between observer and satellite for each simulated light curve timestamp. Furthermore, a detailed 3D CAD model has been provided by the IRS, which is broken down to the relevant outer structure parts, shown in Fig. 6.

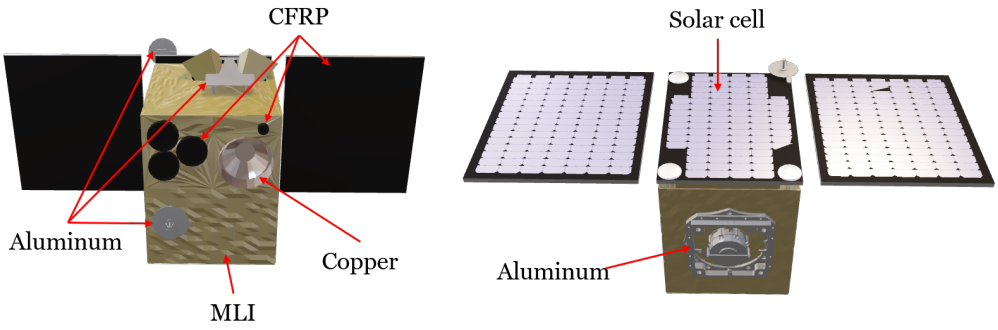

Fig. 6: Model of the Flying Laptop satellite used for the simulations.

Each material, in terms of their BRDF (see subsection 2.3), is assigned to the corresponding mesh surface, with respect to their reflectance spectra from Fig. 2 and Beckmann slope α, as listed in Table 1.

3.2 Observations

Light curves of the Flying Laptop have been observed with the former UFO and the miniSLR. Both were designed as SLR (Satellite Laser Ranging) stations at the DLR in Stuttgart. The UFO is no longer in operation. The miniSLR follows the concept of an accurate, small, lightweight, and cost-efficient SLR station that can be distributed around the globe [27]. It is currently placed on the roof top of the DLR institute in Stuttgart. Both stations were equipped with an Andor Zyla 5.5 camera sensor, with a resolution of 2560 x 2160 pixel at the time of the observations. The individual receiver specifications are listed in Table 2.

Table 2: DLR Institute of Technical Physics ground stations

Parameter	UFO	miniSLR
Telescope	Planewave CDK 17	ASA Astrograph 8" H
Aperture size	43 cm	20 cm
Field of View	$0.32° \times 0.27°$	$0.92° \times 0.69°$

Measurements are taken as a series of images of the tracked object, typically with an integration time of 1 s.

The measurements of absolute intensities are gained as integrated digital counts of the collected pixel brightness of the object in a dedicated RoI (Region of Interest), divided by the integration time of the sensor, resulting in a sensor count

rate. Further, the intensities are corrected by the mean background flux of the surrounding annulus of the object. An example image snapshot, including the RoI and annulus used for brightness extraction, is shown in Fig. 7.

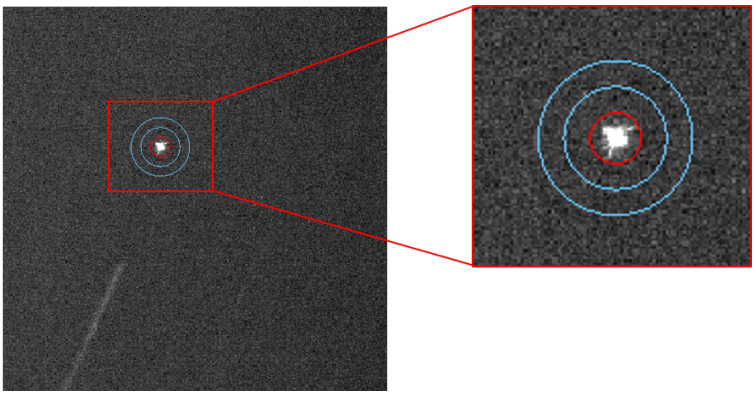

Fig. 7: Exemplary tracking image of the Flying Laptop satellite for the brightness extraction, including the RoI (red) surrounding the target and the annulus (blue) for background subtraction.

4. RESULTS AND DISCUSSION

This section gives an overview of the results that were found for the simulated and measured light curve passes. The findings are discussed, pointing out possible induced errors and uncertainties. Subsequently, the reflectivity maps and projected measurements of the Flying Laptop satellite are shown. Furthermore, light curve extraction from the reflectivity map is demonstrated and discussed, essentially paving the way for fast light curve assessment.

4.1 Simulation validation

First, a comparison of measured and simulated light curves is shown and discussed. For this purpose, several light curves of Flying Laptop passes have been simulated using the measured material BRDFs presented in subsection 2.3. In Fig. 8 the measured light curves from the UFO and the miniSLR, including the corresponding simulations are shown.

The light curves are plotted as absolute integrated radiometric sensor count rate, as elaborated above, over the time of the start epoch of the pass. Instrumental uncertainties of the measured signal are considered as the variation of SNR (Signal to Noise Ratio), which is added to the signal (see [28] for computational details). The instrumental uncertainty is provided as shaded blue area along the measurement curve, clearly visible in the miniSLR pass on the bottom right of Fig. 8. Simulations are generated in the same manner, assuming no background flux and no instrumental uncertainties.

It can be seen that the structure and the relative values of the simulated light curves corresponds well with the measured ones, emphasizing the comparable gradients of the intensities during the passes. In addition, the features that are visible in the first half of the UFO passes and in the end of the miniSLR pass in the bottom row of the figure, are comparably reproduced in the simulations. Highlighting the RMS error of one order of magnitude below the mean radiometric sensor response.

Nevertheless, discrepancies of a factor two to three are present for the UFO passes and up to a factor of ten for the miniSLR pass. First, taking a look at the UFO passes reveals a positive offset between measurement and simulation in the first two plots in the upper row of Fig. 8, thus, overestimating the true brightness of the satellite by roughly a factor of two. This discrepancy may originate from local high altitude cirrus clouds during these nights, decreasing the received signal on the sensor. A way to overcome this issue is to perform stellar calibrations by comparing the absolute measured and theoretical counts of stars with known brightness. This factor can then be used to calibrate the measured intensities of the satellites. [19] shows that this can make up a factor of roughly 0.5 between measurement and theoretical star counts, which corresponds to the current offset. Unfortunately no star images are available for these observations.

Deviations of the gradients and missing features, such as in top row of Fig. 8, may be induced due to a non-perfect model of the satellite and the reflection properties of the materials under certain viewing angle conditions. The current

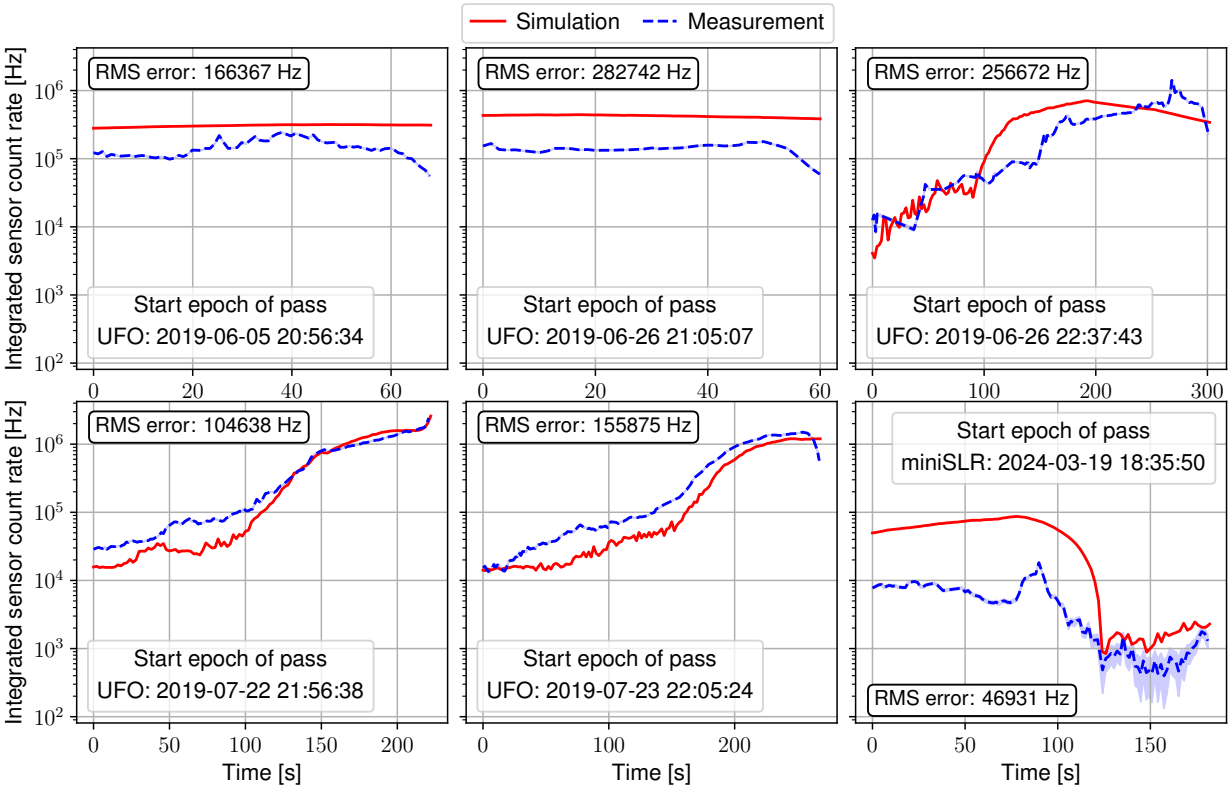

Fig. 8: Measured (blue) and simulated (red) light curves of the Flying Laptop satellite for the UFO and the miniSLR, respectively. Additionally, the RMS error between measurement and simulation is displayed. Instrumental uncertainties [28] are provided as blue shaded area.

materials are all assumed to be isotropic, which is essentially not the case for CFRP. This may lead to incorrect reflection lobes for specific phase and observation angles, depending on the orientation of the satellite. Furthermore, the MLI hull of the satellite was modeled in a way to represent the creased structure of the foil by tilting random polygons of the mesh by a few degrees. This does not have to correspond to the actual texture of the MLI foil, but is a first step to represent it in a realistic manner, increasing the probability for specular reflections for a wider range of phase angles, in comparison to a planar surface structure.

Moving on to the miniSLR pass, it can be seen that the features and brightness of the light curve within the first 120 s do not meet the measurement. This may be caused due to environmental conditions, e.g., local cirrus clouds, reducing the measured signal or by an incorrect representation of the wavelength-dependent system throughput. The miniSLR system is currently undergoing frequent opto-mechanical changes, which is why a full characterization of the system throughput is impeded. This will be tackled in the future, once it has reached a stable configuration.

In terms of experimental studies, following uncertainties occur due to the laboratory measurements of the materials. First of all, the measured spectra are corrected by a reference gold curve, which focuses the light onto the sensor. The gold spectra is generated via Fresnel equations and may not fully correspond to the actual spectra. Errors in the measured spectra may also occur, if the sample is not clamped fully planar, e.g., in the case of the MLI, which has a crumpled structure. Furthermore, the extraction of the Beckmann slopes from the roughness measurements strongly depends on where the sample was measured, and also neglects macroscopic features.

4.2 Reflectivity maps

A method that shows promise in enhancing our understanding of targets surface composition and motion was employed by Kucharski et al. in their works [29, 30]. This method involves projecting measured light curve data points onto a sphere within a target's body frame, allowing for the creation of a reflection map. The position of measurements on this map is determined by the orientation of the data's corresponding phase vector relative to the target's body frame,

illustrated on the left in Fig. 9. In their work, Kucharski et al. matched the projected measurements fingerprints, such as specular reflections to biometric markers of the satellite by fitting the rotational axis. If the fit coincides well with the real rotation of the object, the projection produces smooth maps and prominent features (see [30] for details).

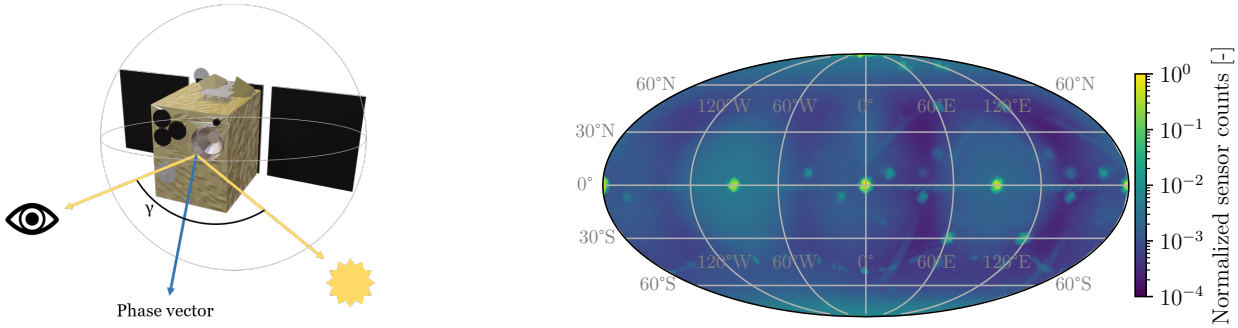

Fig. 9: **Left:** Projection of the phase vector into a body fixed frame, including the phase angle γ. **Right:** Fully simulated reflectivity map for a generic observer based on [29, 30]. Observer and Sun are co-aligned ($\gamma = 0$).

Since these maps are unique for each target, we extend the method described by Kucharski et al. [29, 30] and fully simulate a known target's reflectivity map for a full rotation of the phase vector in the body frame. This is exemplary done for the Flying Laptop satellite, shown on the right in Fig. 9. The phase vector is hereby mapped by latitude and longitude angles. Certain viewing directions, i.e., parallel to the surface normals, produce specular reflections, resulting in prominent features in the map, e.g., by the MLI or the solar cells. Our method employs the assumption that the light source, i.e., the Sun, and observer are co-aligned ($\gamma = 0$), thus, the incident and outgoing directions of light are assumed to match the phase vector at every point. We also discard atmospheric attenuation, assume that the observer is in arbitrarily close distance to the target, and further normalize the map data by their maximum value. These simplifying assumptions are considered for the generation and illustration of a fully simulated map only, but discussed critically in the following where this approach is compared to real-world measurements and pass-specific light curve computations.

In combination with its rotational motion, each pass of a space object produces a trajectory of the phase vector inside the map. While the geometry between observer, Sun, and target and, hence the evolution of the phase vector in an inertial frame is known, the attitude evolution of the object can be derived from the best match of the measured light curve with the related trajectory in the map. A found match reveals the trajectory of the phase vector in the body-fixed frame, thus, resulting in the attitude evolution during the pass. It should be noted, however, that ambiguities are likely to occur during this fitting routine as the space of possible map trajectories covers three degrees of freedom (tumbling discarded), namely rotation axis orientation and angular frequency.

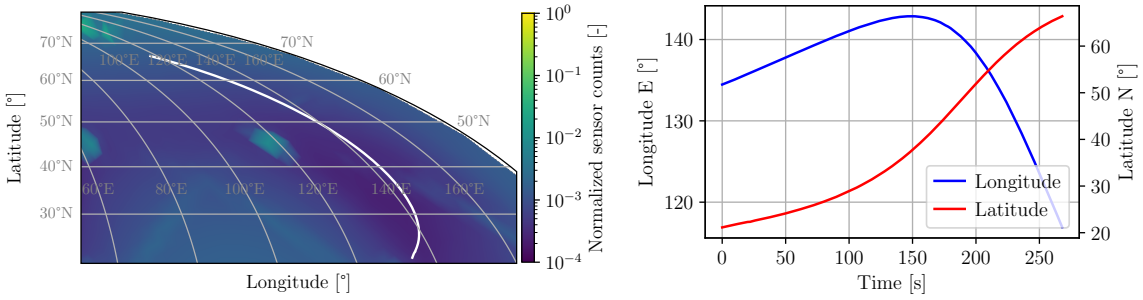

Fig. 10: **Left:** Zoomed in region of the simulated reflectivity map of the Flying Laptop from Fig. 9, including the phase vector (white) trajectory in the body-fixed frame from the UFO pass from the 2023-07-23. **Right:** Corresponding latitude and longitude values of the phase vector in the body-fixed frame.

The conceptual idea of light curve representation within a reflectivity map is shown in Fig. 10 for the UFO pass as of

2024-07-23. Since the map is a large two-dimensional array, it enables fast computation of a light curve estimate, by interpolating the values along a phase vector trajectory. From this, applying the corresponding atmospheric attenuation, orbit ephemerides, and system parameters, the radiometric sensor count rate can be computed. In Fig. 11 the measured, conventionally simulated and from the map interpolated light curves for the UFO pass are displayed. Keep in mind that the generation of the map uses the assumption that the phase angle γ remains at 0° and therefore, discrepancies to the simulation may occur, which are related to the correct phase angle.

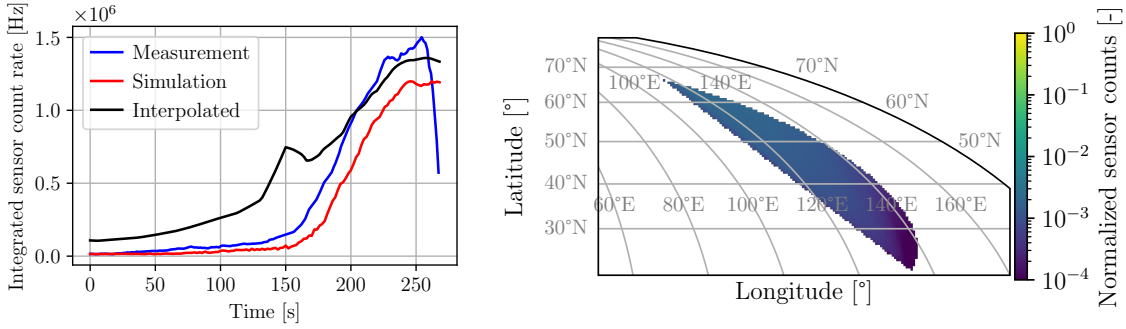

Fig. 11: **Left:** Comparison of measured, conventionally simulated and from the map interpolated light curves for the UFO pass from the 2023-07-23. **Right:** Measurement data projection for the UFO pass (2019-07-23).

The comparison of the three light curves reveals that the interpolated light curve from the simulated map, shows a slight positive offset and a shallower gradient to the simulation. Furthermore, a bright feature is visible at 150 s, which is not apparent in the other light curves. This might originate from the fact that the simulation of the map undergoes the assumption of co-alignment of observer and light source, i.e., $\gamma = 0$. Therefore, the half space of multiple incident and outgoing directions of light for one phase vector is compressed into one value, neglecting divergent phase angles from the measurement. The other passes shown Fig. 8 point out a similar behavior, which will be investigated in the future.

This mapping further reveals, which parts of the object's intensities are covered for certain passes. In our case of the Flying Laptop, the projected measurements only cover a small and similar area on the map, since the satellite is in station pointing during the passes over Stuttgart. In result, lots of features of the reflectivity map remain unrevealed. Therefore, this technique is illustrated only for one of the passes, shown on the right of Fig. 11.

Nevertheless, it shows that this method has the potential for fast light curve analysis, which will be further investigated. In the future, light curves for various orientations, by commanding dedicated attitude control modes, will be measured for the Flying Laptop for this purpose. This enables the quantification of the exploited reflectivity maps and pads further intensity areas inside unseen parts of the map.

5. CONCLUSION AND OUTLOOK

In this study we have analyzed the performance of our light curve simulation software, Raxus Prime, for a complex satellite shape and material distribution and validated it against measured Flying Laptop light curves. Simulations are incorporated with an analytical BRDF model, using spectral and roughness laboratory measurements of the integrated materials. Absolute measured quantities are met within a RMS error of one order of magnitude below the mean sensor response between measurement and simulation. Partial simulations indicate discrepancies, which may be caused due to environmental conditions, a non-perfect model of the satellite, and the materials reflectance characteristics.

In further research, we plan to set up a database containing BRDF data of commonly applied space materials including satellite and rocket stage materials and incorporate data from BRDF measurements into the simulation. This would allow for eliminating limitations due to calculated BRDF from micro-facet theory as well as the requirement of measuring roughness maps per material in addition to a reflectance spectrum. Furthermore, measured BRDFs are essentially angle-resolved spectral reflectance measurements which reduces the computational effort. This would combine the findings of the present study with the results of [14] and allow for high-fidelity reflectivity maps based

on real satellite material BRDFs, further minimizing errors in potential attitude determination as well as in orbital material characterization.

In order to get in-depth knowledge of the reflectivity maps and the true intensity distribution for a wider range of phase angles, commanded passes with defined rotations are planned with the Flying Laptop satellite. Furthermore, stellar calibrations will be performed with the miniSLR for future measurements, reducing the discrepancies of simulation and measurement, in combination with measured BRDFs.

REFERENCES

[1] European Space Agency, "ESA's annual Space Environment Report 2023," tech. rep., ESOC, Robert-Bosch-Straße 5, D-64293 Darmstadt, Germany, 2023.

[2] European Space Agency, "Space debris by the numbers." `https://www.esa.int/Space_Safety/Space_Debris/Space_debris_by_the_numbers`, July 2024.

[3] T. Kelso, "Analysis of the Iridium 33 - Cosmos 2251 collision," *Advances in the Astronautical Sciences*, vol. 135, no. 2, pp. 1099–1112, 2009.

[4] T. J. Muelhaupt, M. E. Sorge, J. Morin, and R. S. Wilson, "Space traffic management in the new space era," *Journal of Space Safety Engineering*, vol. 6, no. 2, pp. 80–87, 2019.

[5] T. Schildknecht, "Optical surveys for space debris," *The Astronomy and Astrophysics Review*, vol. 14, pp. 41–111, 2007.

[6] N. Adilov, V. Braun, P. Alexander, and B. Cunningham, "An estimate of expected economic losses from satellite collisions with orbital debris," *Journal of Space Safety Engineering*, vol. 10, no. 1, pp. 66–69, 2023.

[7] T. J. Colvin, J. Karcz, and G. Wusk, "Cost and Benefit Analysis of Orbital Debris Remediation," tech. rep., NASA, March 2023.

[8] C. Blackerby, A. Okamoto, S. Iizuka, Y. Kobayashi, K. Fujimoto, Y. Seto, S. Fujita, T. Iwai, N. Okada, J. Forshaw, *et al.*, "The ELSA-d end-of-life debris removal mission: preparing for launch," in *Proceedings of the 70th International Astronautical Congress, IAC*, vol. 8, 2019.

[9] R. Biesbroek, S. Aziz, A. Wolahan, S. Cipolla, M. Richard-Noca, and L. Piguet, "The Clearspace-1 mission: ESA and clearspace team up to remove debris," in *Proc. 8th European Conference on Space Debris*, pp. 1–3, 2021.

[10] A. Willison and D. Bédard, "Light curve simulation using spacecraft CAD models and empirical material spectral BRDFs," in *Proceedings of the Advanced Maui Optical and Space Surveillance Technologies Conference, Maui, HI, USA*, pp. 15–18, 2015.

[11] A. Petit, H. Tarrieu, L. Duthil, A. Rolin, and D. Giolito, "Light curve model validation by cross-comparison with photometric data for space object characterisation," in *2nd NEO and Debris Detection Conference*, p. 65, 2023.

[12] H. Wang, W. Zhang, and A. Dong, "Modeling and validation of photometric characteristics of space targets oriented to space-based observation," *Applied Optics*, vol. 51, no. 32, pp. 7810–7819, 2012.

[13] S. Klinkner, S. Gaisser, J. Keim, K.-S. Klemich, L. Michael, and U. Mohr, "Stuttgart university's reliable, high-performance small satellite platform on its first mission" flying laptop," in *Proceedings of the 12th IAA Symposium on Small Satellites for Earth Observation*, 2019.

[14] M. Nussbaum, E. Schafer, Z. Yoon, D. Keil, and E. Stoll, "Spectral light curve simulation for parameter estimation from space debris," *Aerospace*, vol. 9, no. 8, p. 403, 2022.

[15] K.-S. Klemich, J. Keim, N. Bucher, J. Burgdorf, M. Böttcher, S. Wenzel, U. Mohr, B. Bätz, S. Gaißer, P. Hagel, *et al.*, *The Flying Laptop University Satellite Mission: Ground Infrastructure and Operations after one Year in Orbit*. 2018.

[16] P. B. Johnson and R.-W. Christy, "Optical constants of the noble metals," *Physical review B*, vol. 6, no. 12, p. 4370, 1972.

[17] D. Burandt, "Simulation of the light curves of orbital objects and comparison with measurements," bachelor thesis, University of Stuttgart, Jan. 2017. German title: Simulation der Lichtkurven orbitaler Objekte und Vergleich mit Messungen.

[18] E. Schafer, "Stereoscopic Light Curve Analysis of Space Debris Objects," master thesis, Julius-Maximilians Universität Würzburg, Lulea Tekniska Universitet, Dec. 2017.

[19] M. Nussbaum, "Simulation and measurement of multispectral space debris light curves," Master's thesis, Technische Universität Berlin, November 2021.

[20] M. Nimier-David, D. Vicini, T. Zeltner, and W. Jakob, "Mitsuba 2: A retargetable forward and inverse renderer," *Transactions on Graphics (Proceedings of SIGGRAPH Asia)*, vol. 38, Dec. 2019.
[21] B. Mayer, A. Kylling, C. Emde, R. Buras-Schnell, U. Hamann, J. Gastgeier, and B. Richter, *libRadtran user's guide*. Deutsches Zentrum für Luft- und Raumfahrttechnik, 2020.
[22] M. Pharr, W. Jakob, and G. Humphreys, *Physically based rendering: From theory to implementation*. MIT Press, 2023.
[23] B. Walter, S. R. Marschner, H. Li, and K. E. Torrance, "Microfacet models for refraction through rough surfaces.," *Rendering techniques*, 2007.
[24] E. Gadelmawla, M. Koura, T. Maksoud, I. Elewa, and H. Soliman, "Roughness parameters," *Journal of Materials Processing Technology*, vol. 123, pp. 133–145, 04 2002.
[25] H. Ragheb and E. R. Hancock, "The modified Beckmann–Kirchhoff scattering theory for rough surface analysis," *Pattern Recognition*, vol. 40, no. 7, pp. 2004–2020, 2007.
[26] "Space-Track." `https://www.space-track.org/`. [Last Access: 14 July 2024].
[27] D. Hampf, F. Niebler, T. Meyer, and W. Riede, "The miniSLR: a low-budget, high-performance satellite laser ranging ground station," *Journal of Geodesy*, vol. 98, January 2024.
[28] P. Castro, T. Payne, V. C. Frey, K. K. Kinateder, and T. J. Godar, "Calculating photometric uncertainty," in *Proceedings of the AMOS Technical Conference*, 2020.
[29] D. Kucharski, G. Kirchner, J. C. Bennett, M. K. Jah, and J. G. Webb, "High-definition photometry—a new tool for space debris characterization," in *Proceedings of the 21st International Workshop on Laser Ranging, Canberra, Australia*, pp. 4–9, 2018.
[30] D. Kucharski, G. Kirchner, M. K. Jah, J. C. Bennett, F. Koidl, M. A. Steindorfer, and P. Wang, "Full attitude state reconstruction of tumbling space debris TOPEX/Poseidon via light-curve inversion with Quanta Photogrammetry," *Acta Astronautica*, vol. 187, pp. 115–122, 2021.

ACKNOWLEDGMENTS

We thankfully acknowledge fruitful scientific discussions with Paul Wagner and Nils Bartels. Furthermore, we want to appreciate Lennart Rauch's and Nicolas Steenbergen's assistance during measurements and data processing. Last but not least, we value Samantha Siegert's great engagement in language editing and spell check.

DECLARATIONS

The authors declare that they have no conflict of interest. Commercial components and software described in the paper were found to be well-suited for our specific purposes, without implying any endorsement or promotion by the authors.

LIST OF ABBREVIATIONS

AIS	Automatic Identification System
AOI	Angle of Incidence
AOR	Angle of Reflectance
BRDF	Bidirectional Reflectance Distribution Function
BSDF	Bidirectional Scattering Distribution Function
CFRP	Carbon-Fiber Reinforced Plastic
DDS	Direct Digital Synthesizer
DLR	German Aerospace Center
ESA	European Space Agency
IRS	Institute of Space Systems
MLI	Multi-Layer Insulation
RMS	Root Mean Square
RoI	Region of Interest
SLR	Satellite Laser Ranging

SNR	Signal to Noise Ratio
SSA	Space Situational Awareness
STM	Space Traffic Management
TLE	Two Line Element
UFO	Uhlandshoehe Forschungsobservatorium
WLIM	White Light Interferometer